Neurovascular Uncoupling: Multimodal Imaging Delineates the Acute Effects of 3,4-Methylenedioxymethamphetamine

Tudor M. Ionescu[1], Mario Amend[1], Tadashi Watabe[1,2], Jun Hatazawa[2], Andreas Maurer[1], Gerald Reischl[1,3], Bernd J. Pichler[1,3], Hans F. Wehrl*[1], and Kristina Herfert*[1]

[1]*Werner Siemens Imaging Center, Department of Preclinical Imaging and Radiopharmacy, Eberhard Karls University Tuebingen, Tuebingen, Germany;* [2]*Department of Nuclear Medicine and Tracer Kinetics, Osaka University, Osaka, Japan; and* [3]*Cluster of Excellence iFIT (EXC 2180) "Image Guided and Functionally Instructed Tumor Therapies", University of Tuebingen, Tuebingen, Germany*

Psychedelic compounds such as 3,4-methylenedioxymethamphetamine (MDMA) have attracted increasing interest in recent years because of their therapeutic potential in psychiatric disorders. To understand the acute effects of psychedelic drugs in vivo, blood-oxygenation-level–dependent (BOLD) functional MRI (fMRI) has been widely used. In particular, fMRI studies have suggested that MDMA leads to inhibition of brain activity, challenging previous hypotheses indicating mainly excitatory effects based, among others, on increased metabolism shown by ^{18}F-FDG functional PET (fPET). However, interpretation of hemodynamic changes induced by psychedelics is difficult because of their potent vascular effects. **Methods:** We aimed to delineate the acute effects of MDMA using simultaneous PET/fMRI in rats. For this purpose, hemodynamic changes measured by BOLD fMRI were related to alterations in glucose utilization and serotonin transporter (SERT) occupancy using ^{18}F-FDG fPET/fMRI and ^{11}C-DASB PET/fMRI. **Results:** We show that MDMA induces localized increases in glucose metabolism in limbic projection areas involved in emotional processing. The increased glucose metabolism was accompanied by global cerebral and extracerebral hemodynamic decreases. We further demonstrated a strong correlation between SERT occupancies and regional BOLD reductions after acute MDMA administration. **Conclusion:** Our data indicate that hemodynamic decreases after acute MDMA administration are of a nonneuronal nature and initiate peripherally. Within the brain, MDMA triggers neuronal activation in limbic projection areas, whereas increased serotonin levels induced by SERT blockage cause neurovascular uncoupling through direct vascular effects. Correct understanding of the in vivo mechanism of MDMA not only supports ongoing research but also warrants a reassessment of previous studies on neuronal effects of psychedelics relying on neurovascular coupling and recommends ^{18}F-FDG fPET as a potentially more robust measure for pharmacologic research.

Key Words: methylenedioxymethamphetamine; neurovascular coupling; PET/fMRI; hemodynamics; metabolism; serotonin

J Nucl Med 2023; 64:466–471
DOI: 10.2967/jnumed.122.264391

Psychedelic drugs, including lysergic acid diethylamide, psilocybin, and 3,4-methylenedioxymethamphetamine (MDMA), have recently gained increasing attention because of their potential benefits for treating psychiatric disorders (*1*). MDMA-assisted psychotherapy is currently in a phase 3 clinical trial to treat severe posttraumatic stress disorder, with encouraging initial results (*2*). Research in this area is also increasingly associated with the development of imaging techniques as quantitative biomarkers in addition to behavioral parameters (*1*). To investigate the mechanisms of psychedelic drugs in vivo, MRI methods inferring neuronal activity through neurovascular coupling, such as blood-oxygenation-level–dependent (BOLD) functional MRI (fMRI) and arterial spin labeling, have been widely used (*3–5*). Interestingly, research performed over the last decade using these methods has shown that psychedelic compounds such as MDMA (*3*) and psilocybin (*4*) inhibit brain activity, contradicting previous studies that indicated mainly excitatory effects (*6–9*).

However, the use of hemodynamic methods may be insufficient to understand the effects of psychedelics on neuronal activity. First, psychedelic drugs elicit their effects by strongly affecting one or more neurotransmitter systems (*10*). Thus, it is crucial to evaluate hemodynamic changes in relation to neurotransmitter alterations. Second, in addition to neuronal effects, an increase in neurotransmitters such as serotonin elicited by psychedelic compounds can have potent vascular effects (*11–13*). This aspect is particularly critical for methods based on neurovascular coupling, such as BOLD fMRI and arterial spin labeling. The emergence of hybrid PET/MRI allows simultaneous assessment of brain function at multiple physiologic levels. The combination of PET with pharmacologic MRI can offer important complementary insight on drug mechanisms (*14,15*). Furthermore, recent developments in the administration of ^{18}F-FDG PET via constant infusion (*16*) have paved the way toward functional PET (fPET). fPET enables the imaging of changes in glucose metabolism at a resolution of minutes (*17*), providing a more robust indirect measure of neuronal activity than is possible with fMRI, being largely immune to vascular changes (*16*).

We aimed to exploit the potential of multimodal imaging to characterize the acute effects of MDMA using PET/fMRI. First, we performed ^{18}F-FDG fPET/fMRI to simultaneously determine hemodynamic and metabolic changes elicited by MDMA and thereby elucidate potential inhibitory or excitatory actions of this compound. In a second cohort, we used ^{11}C-3-amino-4-(2-dimethylaminomethylphenylsulfanyl)-benzonitrile (^{11}C-DASB) to investigate relationships between hemodynamic alterations and changes in serotonin transporter (SERT) availability, one of the main targets of MDMA (*18*).

Received May 26, 2022; revision accepted Sep. 14, 2022.
For correspondence or reprints, contact Kristina Herfert (kristina.herfert@med.uni-tuebingen.de).
*Contributed equally this work.
Published online Sep. 29, 2022.

MATERIALS AND METHODS

Animals

Male Lewis rats (n = 29) were obtained from Charles River Laboratories and divided into 2 groups: ^{18}F-FDG fPET/fMRI was performed on 17 animals (body weight, 361 ± 19 g), whereas ^{11}C-DASB PET/fMRI was performed on 11 animals (body weight, 365 ± 19 g). Nine fMRI datasets were excluded from the study because of motion during acquisition. One ^{11}C-DASB PET and two ^{18}F-FDG fPET datasets were excluded from the analysis because of paravenous tracer injections. The animals were kept at a room temperature of 22°C and 40%–60% humidity under a 12-h light–dark cycle. The rats were fed with standard diet and received tap water ad libitum. They were kept fasting for 6 h before the start of the experiments. All experiments were performed in accordance with the German Federal Regulations on the Use and Care of Laboratory Animals and approved by the Tuebingen regional council. Two additional cohorts scanned under the same ^{18}F-FDG fPET/fMRI and ^{11}C-DASB PET/fMRI protocols, but exposed to phosphate-buffered saline instead of MDMA, are presented in the supplemental materials (available at http://jnm.snmjournals.org) (*3–6,10,11,15,16,19–36*).

Simultaneous PET/fMRI Experiments

The animals were scanned under 1.3% isoflurane and constant monitoring of breathing rate and temperature (Supplemental Fig. 1) using a 7-T small-animal MRI scanner (ClinScan; Bruker). T2-weighted anatomic reference scans and fMRI scans (repetition time, 2,000 ms; echo time, 18 ms) were obtained using a linearly polarized radiofrequency coil for transmission and a 4-channel surface rat brain coil for reception. The PET scans were acquired simultaneously using an in-house–developed insert and reconstructed into 100 frames of 1 min using an ordered-subsets expectation-maximization 2-dimensional algorithm. The MDMA challenge (3.2 mg/kg) was applied 40 min after the start of the acquisition. Additional details on the experimental procedure are provided in the supplemental materials.

Data Analysis

Statistical Parametric Mapping (SPM12, Wellcome Trust Centre for Neuroimaging) via Matlab (The MathWorks) and Analysis of Functional NeuroImages (AFNI, National Institute of Mental Health) were used for data preprocessing as previously reported (*37*). An extensive description of all preprocessing and analysis steps can be found in the supplemental materials. Average time courses were extracted from all datasets after preprocessing using the MarsBaR toolbox (*38*) and regions of interest (see Fig. 1 for abbreviations and Supplemental Table 1 for their respective volumes) defined by the atlas of Schiffer et al. (*34*). Additionally, extracerebral BOLD fMRI signals were extracted using binary masks generated with AFNI. The general linear model available in SPM was applied to determine voxels with significantly altered fMRI and PET signals after MDMA exposure. For all datasets, baseline was defined as 30–40 min after the scan start, when tracer equilibrium had been reached between the regions with high SERT density and high ^{18}F-FDG uptake and the reference regions. The ^{18}F-FDG fPET data were normalized using cerebellar uptake. For ^{11}C-DASB PET, the cerebellar gray matter was chosen as the reference region as previously described (*36*). For all methods, the signal at baseline was compared with six 10-min blocks between the challenge (40 min after the scan start) and the end of the scan (100 min after the scan start). Group-level T-maps were generated for all cohorts, methods, and time periods. All T-maps were subjected to voxelwise signal quantification to determine the regional contributions of the brain regions selected. The average T-scores of all voxels comprising each region were calculated for each period and modality to compare the respective spatial patterns of MDMA effects on hemodynamics, glucose metabolism, and SERT occupancy.

RESULTS

Metabolic Increases Accompany Hemodynamic Reductions

First, we investigated the relationship between hemodynamic and metabolic changes after acute MDMA administration using simultaneous ^{18}F-FDG fPET/fMRI (Figs. 1 and 2; Supplemental Fig. 2).

The normalized ^{18}F-FDG fPET time–activity curves for all regions and the average whole-brain time–activity curve and voxelwise uptake maps (Fig. 1A) indicated an increase in metabolism in the midbrain and in the anterior subcortical and frontal cortical areas, whereas more minor or no changes occurred in the posterior cortical regions. Notably, we found a simultaneous decrease in hemodynamics, as indicated by BOLD fMRI (Fig. 1B). The whole-brain–averaged BOLD fMRI signal was reduced by 4.5% 15 min after the challenge. Importantly, the data revealed that the decreases were global and occurred in all regions investigated. A temporal comparison of the ^{18}F-FDG fPET and BOLD signal changes relative to baseline is shown in Figure 1C. The highest metabolic increases occurred in frontal areas, including the caudate putamen (22%), insular cortex (21%), medial prefrontal cortex (18%), and amygdala (13.5%). Increases in all regions (>1%) were observed within 5 min of the challenge.

The voxelwise general-linear-model analyses presented in Figure 2 revealed metabolic

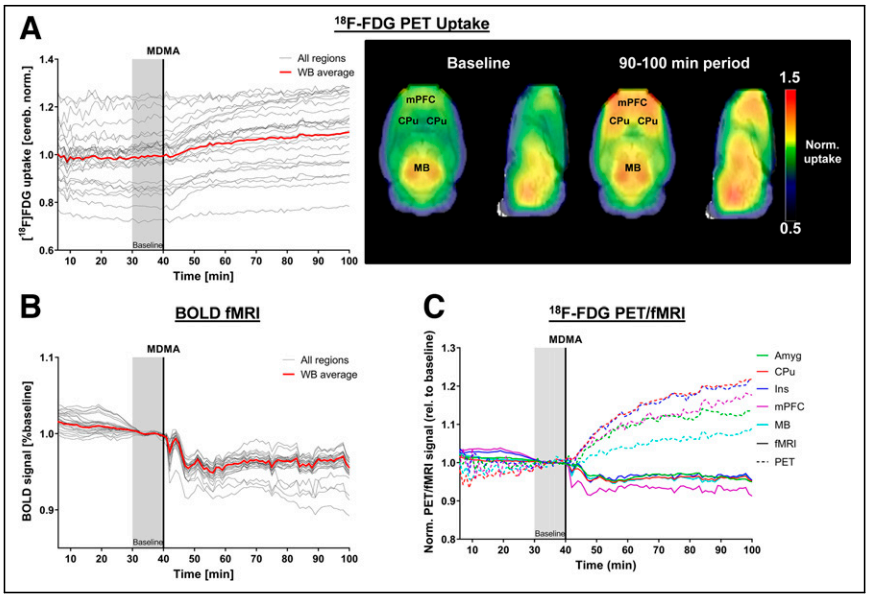

FIGURE 1. Regionwise evaluation of ^{18}F-FDG fPET and BOLD fMRI signal changes. (A) Time–activity curves for all regions and whole-brain average. Voxelwise normalized uptake maps indicate ^{18}F-FDG uptake at baseline and at 90–100 min. (B) Regional BOLD fMRI signals normalized to respective baseline periods. (C) Both signals normalized to baseline period over last 10 min before MDMA administration for common frame of reference. Amyg = amygdala; CPu = caudate putamen; Ins = insular cortex; MB = midbrain; mPFC = medial prefrontal cortex; WB = whole brain.

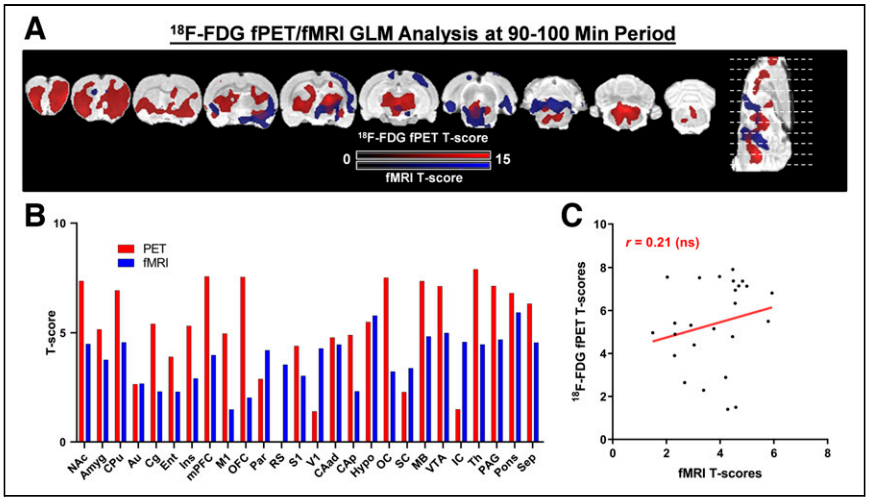

FIGURE 2. General-linear-model analysis of ^{18}F-FDG fPET/fMRI cohort. (A) Voxelwise analysis of both signals at 90–100 min ($P < 0.05$ family-wise error–corrected at voxel level for PET, $P < 0.001$ at voxel level with $P < 0.05$ family-wise error cluster-level correction for fMRI, $n = 15$ for fPET, $n = 9$ for fMRI). (B) Bar diagram indicating average T-scores for each region and modality. (C) Average regional T-scores plotted in scatter diagram to evaluate spatial correlation of both readouts. Amyg = amygdala; Au = auditory cortex; CAad = anterodorsal hippocampus; CAp = posterior hippocampus; Cg = cingulate cortex; CPu = caudate putamen; Ent = entorhinal cortex; GLM = general linear model; Hypo = hypothalamus; IC = inferior colliculus; Ins = insular cortex; M1 = motor cortex; MB = midbrain; mPFC = medial prefrontal cortex; NAc = nucleus accumbens; OC = olfactory cortex; OFC = orbitofrontal cortex; PAG = periaqueductal gray matter; Par = parietal cortex; RS = retrosplenial cortex; S1 = somatosensory cortex; SC = superior colliculus; Sep = septum; Th = thalamus; V1 = visual cortex; VTA = ventral tegmental area.

increases across several subcortical areas and in frontal cortical areas between 90 and 100 min. The medial prefrontal cortex and orbitofrontal cortex (T = 7.6 for both), along with the midbrain (T = 7.4), thalamus (T = 7.9), and nucleus accumbens (T = 7.4), exhibited the most significant ^{18}F-FDG increases. The most significant BOLD fMRI decreases occurred in posterior areas such as the midbrain (T = 4.8), ventral tegmental area (T = 5.0), hypothalamus (T = 5.8), and pons (T = 5.9). The T-scores of metabolic increases and hemodynamic decreases did not correlate significantly ($r = 0.21$).

SERT Occupancy Changes Induced by MDMA Correlate with BOLD Decreases

To further elucidate the molecular underpinnings of the observed hemodynamic decreases, we evaluated BOLD fMRI changes concurrently with alterations in SERT availability using ^{11}C-DASB PET/fMRI in a second cohort (Figs. 3 and 4; Supplemental Fig. 3).

The ^{11}C-DASB nondisplaceable binding potential (BP_{ND}) reached equilibrium 30 min after injection (Fig. 3A). After the challenge, binding in all regions decreased either immediately (1–2 min after the challenge) in areas with high binding values ($BP_{ND} > 1.8$) or with a delay of approximately 10 min in regions with lower ^{11}C-DASB binding values. At 30 min after the challenge, binding remained stable until the end of the scan. Similarly to the ^{18}F-FDG fPET/fMRI cohort, all regional BOLD signals decreased within 6 min after the challenge (Fig. 3B). Regions with higher baseline SERT availability showed a faster response than regions with lower baseline SERT availability (Fig. 3C). For example, ^{11}C-DASB binding in the midbrain ($BP_{ND} = 2.1$) decreased immediately after the challenge. In contrast, ^{11}C-DASB binding in the caudate putamen ($BP_{ND} = 1.6$) and medial prefrontal cortex ($BP_{ND} = 1.6$) remained stable or increased briefly. After approximately 10 min, ^{11}C-DASB binding decreased in all regions until it reached equilibrium at 30–40 min after the challenge (39% decrease for medial prefrontal cortex, 44% decrease for caudate putamen). BOLD decreases occurred homogeneously, peaking 30 min after the challenge (~8.5% in medial prefrontal cortex, ~5.5% in caudate putamen, and ~6.5% in midbrain).

Figure 4 shows the voxelwise decreases at 70–80 min after the scan start. Regional averages showed the strongest decreases in the ventral tegmental area (T = 13.7), periaqueductal gray matter (T = 12.8), and midbrain (T = 12.7) for ^{11}C-DASB and in the hypothalamus (T = 7.8), ventral tegmental area (T = 7.2), and thalamus (T = 6.9) for BOLD fMRI. Remarkably, regional T-scores of both readouts correlated strongly ($r = 0.79$, $P < 0.001$).

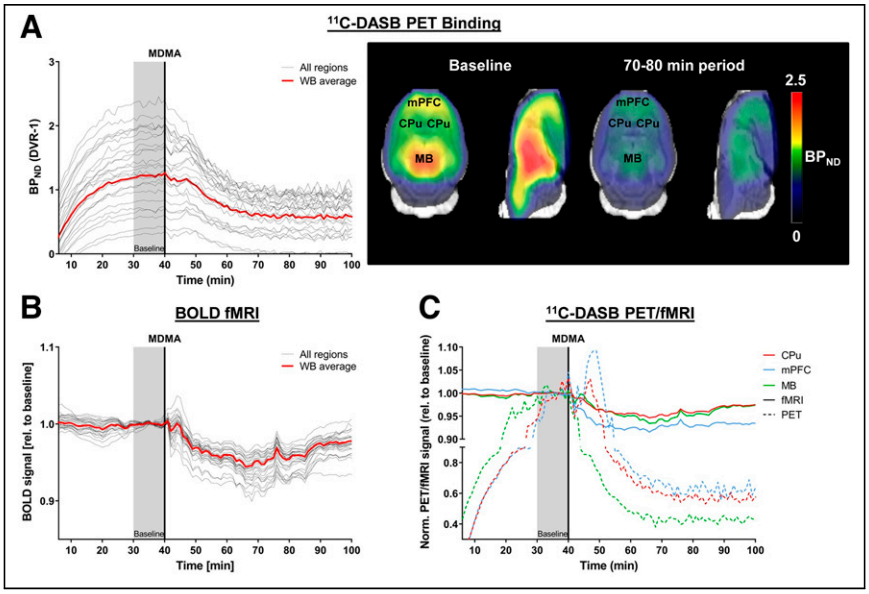

FIGURE 3. Regionwise evaluation of ^{11}C-DASB PET and BOLD fMRI signal changes. (A) Dynamic BP_{ND} for all regions and whole-brain average. Voxelwise maps indicate ^{11}C-DASB binding at baseline, as well as 70–80 min after scan start. (B) Regional BOLD fMRI signals normalized to respective baselines. (C) Temporal comparison of PET and BOLD signal changes (normalized to baseline) in caudate putamen, medial prefrontal cortex, and midbrain. CPu = caudate putamen; DVR = distribution volume ratio; MB = midbrain; mPFC = medial prefrontal cortex; WB = whole brain.

Hemodynamic Reductions Also Occur in Nonneuronal Tissues

The limited spatial extent of hemodynamic changes compared with the metabolic

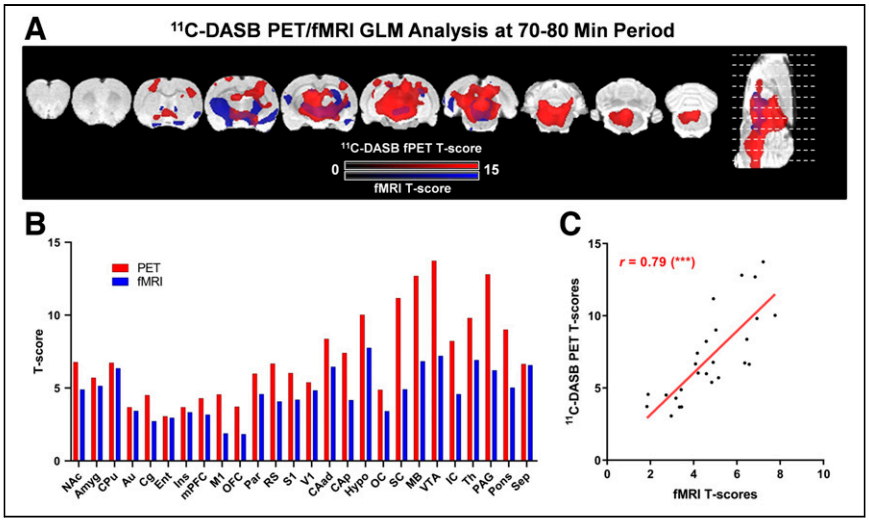

FIGURE 4. General-linear-model analysis of ^{11}C-DASB PET/fMRI cohort. (A) Voxelwise analysis of both signals at 70–80 min. Voxelwise maps are presented ($P < 0.05$, voxel-level family-wise error correction for PET and $P < 0.001$ at voxel level with $P < 0.05$ family-wise error cluster-level correction for fMRI, $n = 11$). (B) Bar diagram indicating average T-scores for each region and modality. (C) Regional T-scores plotted in scatter diagram to evaluate spatial correlation of both readouts. ***$P <$ 0.001. Amyg = amygdala; Au = auditory cortex; CAad = anterodorsal hippocampus; CAp = posterior hippocampus; Cg = cingulate cortex; CPu = caudate putamen; Ent = entorhinal cortex; GLM = general linear model; Hypo = hypothalamus; IC = inferior colliculus; Ins = insular cortex; M1 = motor cortex; MB = midbrain; mPFC = medial prefrontal cortex; NAc = nucleus accumbens; OC = olfactory cortex; OFC = orbitofrontal cortex; PAG = periaqueductal gray matter; Par = parietal cortex; RS = retrosplenial cortex; S1 = somatosensory cortex; SC = superior colliculus; Sep = septum; Th = thalamus; V1 = visual cortex; VTA = ventral tegmental area.

Additional Analyses

Analyses of the phosphate-buffered saline cohort and a comparison with the readouts shown after MDMA application are provided in Supplemental Figures 4–5. Furthermore, we extracted general-linear-model alterations induced by MDMA in each subject of both the ^{11}C-DASB cohort and the ^{18}F-FDG cohort to demonstrate the feasibility of subject-level PET inferences using our approach (Supplemental Figs. 6–7). Additionally, we reproduced the metabolic changes using whole-brain normalization and validated the choice of the cerebellum for normalization (Supplemental Fig. 8). Moreover, we examined the robustness of our correlation between hemodynamic and SERT decreases by using β-values and subject-level general-linear-model readouts (Supplemental Fig. 9). Finally, we compared the temporal characteristics of the observed hemodynamic, metabolic, and SERT availability changes (Supplemental Fig. 10).

DISCUSSION

Our data indicate that increased neuronal activity after MDMA is accompanied by neurovascular uncoupling, possibly mediated through the vascular effects of serotonin after SERT blockage.

and SERT occupancy alterations may be due to the smaller magnitudes of the BOLD decreases. To further clarify this aspect, we merged the fMRI scans from both cohorts (Fig. 5). We also extracted the BOLD signals from extracerebral areas to investigate whether the BOLD decreases are specific to neuronal tissue.

After the cohorts were merged, the BOLD fMRI decreases were widespread and, intriguingly, also occurred in nonneuronal areas (Fig. 5). The average extracerebral BOLD signal decreased coherently with the cerebral BOLD signal, both reaching maximum reductions 27 min after the challenge (cerebral BOLD, 4.8%; extracerebral BOLD, 7.4%).

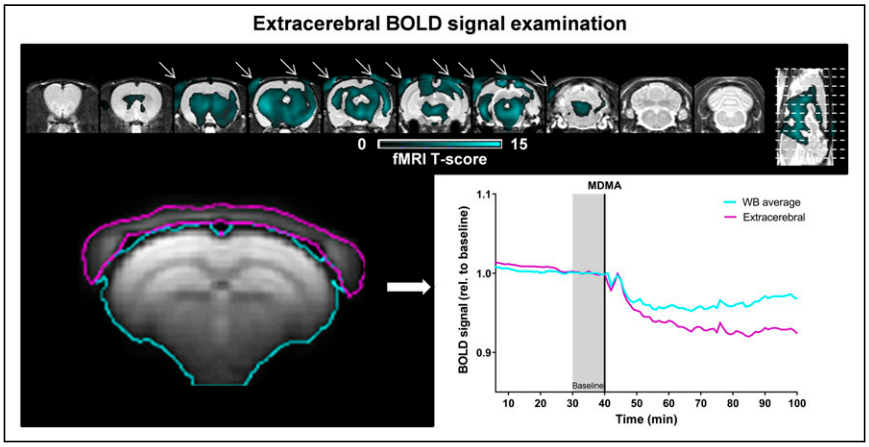

FIGURE 5. General-linear-model analysis of BOLD decreases after merging BOLD fMRI datasets acquired in both cohorts ($n = 20$). Data are shown at $P < 0.05$, family-wise error–corrected at voxel level. Arrows indicate extracerebral decreases. Average BOLD signals were extracted from extracerebellar regions and plotted along with whole-brain signal. WB = whole brain.

Simultaneous Uncoupling Between Metabolism and Hemodynamics

Studies measuring glucose utilization after psychedelic challenges have shown mixed results, yet the main result has been increased metabolism (*6,7,9,35*), suggesting neuronal activation. However, more recent work performed by Carhart-Harris et al. (*3*), using arterial spin labeling challenged this hypothesis and argued that brain activity is exclusively decreased solely under MDMA. Our study confirmed that this finding also holds true in rodents. Carhart-Harris et al. speculated that MDMA exerts inhibitory effects directly through serotonin receptor (5-HT) 1A (*3,39*). Comparable reductions under acute psilocybin reported by the group of Carhart-Harris were attributed to the inhibitory effects of 5-HT2A receptors (*4*). On a side note, the hemodynamic decreases for MDMA and psilocybin in humans were located predominantly in the right hemisphere (*3,4*), similarly to our study, thereby supporting the translatability of our readout. Notably, Carhart-Harris et al. argued that possible discrepancies with previous work indicating increased metabolism using ^{18}F-FDG PET (*9*) might be due to its inferior temporal resolution (*4*). Therefore, the authors claimed that the reported increases may represent a rebound in glucose metabolism after the acute inhibition captured by fMRI (*4*). We agree that earlier ^{18}F-FDG PET or ex vivo studies (*6,7,9,35*) measuring cerebral glucose utilization lacked temporal specificity because

of methodologic limitations on their interpretability in terms of acute effects. An additional confound is that the studies compared different, relatively small cohorts having received either placebo or MDMA. The present work overcomes all these limitations. The constant-infusion protocols used for both tracers enabled delineation of pharmacologic effects immediately after the challenge at 1-min intervals, simultaneously with hemodynamic alterations, and within the same subjects. Therefore, we demonstrated that the uncoupling between flow and metabolism previously shown (*6,11,35*) does occur simultaneously within the same subjects.

Origin of Peripheral and Cerebral Hemodynamic Decreases

We showed that nonneuronal effects dominate hemodynamic changes induced by MDMA. In particular, our data shed light on 2 separate phenomena. First, the temporal coherence between hemodynamic reductions in cerebral and extracerebral areas suggests that vascular effects occur at the periphery. The 5-HT2A receptor, which is postulated—along with the 5-HT1B receptor—to mediate vasoconstrictive effects (*40,41*), is one of the main targets of MDMA (*5,42*). However, because MDMA has a much stronger affinity to the 5-HT2A receptor than to the 5-HT1B receptor (*5*), direct agonist action of MDMA at 5-HT2A in peripheral blood vessels likely drives our results (*40*). Previous work has demonstrated the role of 5-HT2A in vasoconstriction of the carotid artery, the main vessel supplying blood to the brain (*43,44*). In addition to peripheral effects, the cerebral hemodynamic decreases are also likely of a serotonergic nature. Existing publications have indicated that serotonin impacts brain hemodynamics (*12,13*) and that direct manipulation of the raphé nuclei constricts cerebral microvasculature (*11*). In contrast to the peripheral hemodynamic reductions, which can be attributed solely to the direct effects of MDMA, the decreases in the brain may additionally be triggered by increased synaptic serotonin levels after SERT blockage. This finding is supported by the high correlation between SERT blockage and hemodynamic decreases in BOLD fMRI, suggesting that increased levels of endogenous serotonin may modulate cerebral hemodynamics. The exact involvement of different receptors needs to be investigated, for instance by combining psychedelic challenges with respective antagonists. Our results warrant a reevaluation of previous data (*3,4*) and generally call for caution when interpreting findings relying on neurovascular coupling under pharmacologic challenges (*3,5,42*).

Anatomy and Physiology of Increased Metabolism

We demonstrated that MDMA increases the metabolism of different regions, likely because of neuronal activation, as fPET has been shown to reliably map onto neuronal activity while being independent of hemodynamic changes (*16*). Interestingly, the metabolic increases were more weighted toward serotonergic projection areas than toward the midbrain regions showing the strongest reductions in SERT availability. First, this finding is in line with the hypothesis that most of the glucose is consumed postsynaptically (*45*). Second, the areas showing increased metabolism are consistent at a functional level with most previously reported behavioral effects of MDMA. The signals observed in the nucleus accumbens, amygdala, and insula align well with salience changes known from imaging and behavioral studies (*3,46*). In particular, the nucleus accumbens is involved in responses to numerous drugs (*47*). The amygdala, insula, and orbitofrontal cortex are strongly involved in emotional processes (*48*). Activity in the olfactory cortex and olfactory bulb could indicate increased food-seeking or sexual arousal (*49,50*). Enhanced metabolic activity in the sensory cortices is in concordance with heightened sensations elicited by MDMA (*49*). Furthermore, the 5-HT2A receptor exhibits a strong anterior–posterior gradient in the cortex, being strongly expressed in frontal areas of the cortex (*51*) and overlapping with the activations indicated by fPET, and has been shown to be responsible for serotonergic activation in projection areas such as the prefrontal cortex (*52*).

Other factors may play a role in the findings, and there are also certain limitations that need to be considered when contemplating our data. The supplemental materials provide a thorough discussion of these aspects.

CONCLUSION

The present study showed the potential of multimodal imaging in drug research. We demonstrated the acute neurovascular uncoupling induced by MDMA, characterized by increased neuronal activity in monoaminergic projection areas and accompanied by vascular depression of a serotonergic nature. Our results provide important insight into the mechanism of action of MDMA and pave the way for the application of ^{18}F-FDG fPET and hybrid fPET/fMRI in drug research.

DISCLOSURE

This research was supported by funds from the Eberhard Karls University Tübingen Faculty of Medicine (fortüne 2209-0-0 and 2409-0-0) to Hans Wehrl, from the Carl Zeiss Foundation to Kristina Herfert, and from the Werner Siemens Foundation to Bernd J. Pichler, as well as by an international exchange grant from the Osaka Medical Research Foundation for Intractable Diseases to Tadashi Watabe. No other potential conflict of interest relevant to this article was reported.

ACKNOWLEDGMENTS

We acknowledge Julia Mannheim, Rebecca Rock, Neele Hübner, Andreas Dieterich, Ines Herbon, Stacy Huang, Sandro Aidone, Linda Schramm, and the Radiopharmacy Department for their administrative and technical support. The graphical abstract was generated using BioRender. This work is part of the PhD thesis of Tudor M. Ionescu.

KEY POINTS

QUESTION: What are the effects of acute administration of MDMA on neuronal activation in the brain?

PERTINENT FINDINGS: Global decreases in BOLD fMRI are of a vascular, rather than a neuronal, nature and strongly correlate with SERT occupancy measured simultaneously using ^{11}C-DASB. In contrast, ^{18}F-FDG fPET indicates simultaneous increases in limbic glucose consumption, potentially mapping onto neuronal activation.

IMPLICATIONS FOR PATIENT CARE: The study emphasizes the caveats of BOLD fMRI and other hemodynamic methods when strong vascular effects are present and recommends the use of ^{18}F-FDG fPET as an alternative for tracking neuronal activity in vivo after pharmacologic challenges in drug research.

REFERENCES

1. Andersen KAA, Carhart-Harris R, Nutt DJ, Erritzoe D. Therapeutic effects of classic serotonergic psychedelics: a systematic review of modern-era clinical studies. *Acta Psychiatr Scand.* 2021;143:101–118.

2. Mitchell JM, Bogenschutz M, Lilienstein A, et al. MDMA-assisted therapy for severe PTSD: a randomized, double-blind, placebo-controlled phase 3 study. *Nat Med.* 2021;27:1025–1033.
3. Carhart-Harris RL, Murphy K, Leech R, et al. The effects of acutely administered 3,4-methylenedioxymethamphetamine on spontaneous brain function in healthy volunteers measured with arterial spin labeling and blood oxygen level–dependent resting state functional connectivity. *Biol Psychiatry.* 2015;78:554–562.
4. Carhart-Harris RL, Erritzoe D, Williams T, et al. Neural correlates of the psychedelic state as determined by fMRI studies with psilocybin. *Proc Natl Acad Sci USA.* 2012;109:2138–2143.
5. Dipasquale O, Selvaggi P, Veronese M, Gabay AS, Turkheimer F, Mehta MA. Receptor-enriched analysis of functional connectivity by targets (REACT): a novel, multimodal analytical approach informed by PET to study the pharmacodynamic response of the brain under MDMA. *Neuroimage.* 2019;195:252–260.
6. Quate L, McBean DE, Ritchie IM, Olverman HJ, Kelly PAT. Acute methylenedioxymethamphetamine administration: effects on local cerebral blood flow and glucose utilisation in the dark agouti rat. *Psychopharmacology (Berlin).* 2004;173:287–295.
7. Soto-Montenegro ML, Vaquero JJ, Arango C, Ricaurte G, García-Barreno P, Desco M. Effects of MDMA on blood glucose levels and brain glucose metabolism. *Eur J Nucl Med Mol Imaging.* 2007;34:916–925.
8. Wilkerson G, London ED. Effects of methylenedioxymethamphetamine on local cerebral glucose utilization in the rat. *Neuropharmacology.* 1989;28:1129–1138.
9. Vollenweider FX, Leenders KL, Scharfetter C, Maguire P, Stadelmann O, Angst J. Positron emission tomography and fluorodeoxyglucose studies of metabolic hyperfrontality and psychopathology in the psilocybin model of psychosis. *Neuropsychopharmacology.* 1997;16:357–372.
10. Gough B, Ali SF, Slikker W, Holson RR. Acute effects of 3,4-methylenedioxymethamphetamine (MDMA) on monoamines in rat caudate. *Pharmacol Biochem Behav.* 1991;39:619–623.
11. Cohen Z, Bonvento G, Lacombe P, Hamel E. Serotonin in the regulation of brain microcirculation. *Prog Neurobiol.* 1996;50:335–362.
12. Kim JG, Leem Y-E, Kwon I, Kang J-S, Bae YM, Cho H. Estrogen modulates serotonin effects on vasoconstriction through Src inhibition. *Exp Mol Med.* 2018;50:1–9.
13. Van Nueten JM, Janssens WJ, Vanhoutte PM. Serotonin and vascular reactivity. *Pharmacol Res Commun.* 1985;17:585–608.
14. Hansen HD, Mandeville JB, Sander CY, et al. Functional characterization of 5-HT(1B) receptor drugs in nonhuman primates using simultaneous PET-MR. *J Neurosci.* 2017;37:10671–10678.
15. Sander CY, Hooker JM, Catana C, et al. Neurovascular coupling to D2/D3 dopamine receptor occupancy using simultaneous PET/functional MRI. *Proc Natl Acad Sci USA.* 2013;110:11169–11174.
16. Villien M, Wey H-Y, Mandeville JB, et al. Dynamic functional imaging of brain glucose utilization using fPET-FDG. *Neuroimage.* 2014;100:192–199.
17. Rischka L, Gryglewski G, Pfaff S, et al. Reduced task durations in functional PET imaging with [^{18}F]FDG approaching that of functional MRI. *Neuroimage.* 2018;181:323–330.
18. Morefield KM, Keane M, Felgate P, White JM, Irvine RJ. Pill content, dose and resulting plasma concentrations of 3,4-methylendioxymethamphetamine (MDMA) in recreational 'ecstasy' users. *Addiction.* 2011;106:1293–1300.
19. Disselhorst JA, Newport DF, Schmid AM, et al. NEMA NU 4-2008 performance evaluation and MR compatibility tests of an APD-based small animal PET-insert for simultaneous PET/MR imaging. *Phys Med Biol.* 2022;67.
20. Solbach C, Reischl G, Machulla H-J. Determination of reaction parameters for the synthesis of the serotonin transporter ligand [^{11}C]DASB: application to a remotely controlled high yield synthesis. *Radiochim Acta.* 2004;92:341–344.
21. Wilson AA, Ginovart N, Schmidt M, Meyer JH, Threlkeld PG, Houle S. Novel radiotracers for imaging the serotonin transporter by positron emission tomography: synthesis, radiosynthesis, and in vitro and ex vivo evaluation of ^{11}C-labeled 2-(phenylthio)araalkylamines. *J Med Chem.* 2000;43:3103–3110.
22. Hamacher K, Coenen HH, Stocklin G. Efficient stereospecific synthesis of no-carrier-added 2-[^{18}F]-fluoro-2-deoxy-D-glucose using aminopolyether supported nucleophilic substitution. *J Nucl Med.* 1986;27:235–238.
23. López-González FJ, Silva-Rodríguez J, Paredes-Pacheco J, et al. Intensity normalization methods in brain FDG-PET quantification. *Neuroimage.* 2020;222:117229.
24. Hodkinson DJ, de Groote C, McKie S, Deakin JFW, Williams SR. Differential effects of anaesthesia on the phMRI response to acute ketamine challenge. *Br J Med Med Res.* 2012;2:373–385.
25. Wehrl HF, Hossain M, Lankes K, et al. Simultaneous PET-MRI reveals brain function in activated and resting state on metabolic, hemodynamic and multiple temporal scales. *Nat Med.* 2013;19:1184–1189.
26. Ionescu TM, Amend M, Hafiz R, et al. Elucidating the complementarity of resting-state networks derived from dynamic [^{18}F]FDG and hemodynamic fluctuations using simultaneous small-animal PET/MRI. *Neuroimage.* 2021;236:118045.
27. Brodde OE. Vascular dopamine receptors: demonstration and characterization by in vitro studies. *Life Sci.* 1982;31:289–306.
28. Passie T, Seifert J, Schneider U, Emrich HM. The pharmacology of psilocybin. *Addict Biol.* 2002;7:357–364.
29. Hutchison RM, Hutchison M, Manning KY, Menon RS, Everling S. Isoflurane induces dose-dependent alterations in the cortical connectivity profiles and dynamic properties of the brain's functional architecture. *Hum Brain Mapp.* 2014;35:5754–5775.
30. Spangler-Bickell MG, de Laat B, Fulton R, Bormans G, Nuyts J. The effect of isoflurane on ^{18}F-FDG uptake in the rat brain: a fully conscious dynamic PET study using motion compensation. *EJNMMI Res.* 2016;6:86.
31. Martínez-Maestro M, Labadie C, Möller HE. Dynamic metabolic changes in human visual cortex in regions with positive and negative blood oxygenation level-dependent response. *J Cereb Blood Flow Metab.* 2019;39:2295–2307.
32. Schaller B, Mekle R, Xin L, Kunz N, Gruetter R. Net increase of lactate and glutamate concentration in activated human visual cortex detected with magnetic resonance spectroscopy at 7 tesla. *J Neurosci Res.* 2013;91:1076–1083.
33. Amend M, Ionescu TM, Di X, Pichler BJ, Biswal BB, Wehrl HF. Functional resting-state brain connectivity is accompanied by dynamic correlations of application-dependent [^{18}F]FDG PET-tracer fluctuations. *Neuroimage.* 2019;196:161–172.
34. Schiffer WK, Mirrione MM, Biegon A, Alexoff DL, Patel V, Dewey SL. Serial microPET measures of the metabolic reaction to a microdialysis probe implant. *J Neurosci Methods.* 2006;155:272–284.
35. Ferrington L, Kirilly E, McBean DE, Olverman HJ, Bagdy G, Kelly PAT. Persistent cerebrovascular effects of MDMA and acute responses to the drug. *Eur J Neurosci.* 2006;24:509–519.
36. Walker M, Ehrlichmann W, Stahlschmidt A, Pichler BJ, Fischer K. In vivo evaluation of ^{11}C-DASB for quantitative SERT imaging in rats and mice. *J Nucl Med.* 2016;57:115–121.
37. Amend M. *Multifunctional PET/MR Imaging Decodes Brain Function on Hemodynamic and Metabolic scales.* Dissertation. Eberhard Karls Universität Tübingen; 2019.
38. Brett M, Anton J-L, Valabregue R, Poline J-B. Region of interest analysis using an SPM toolbox [abstract]. *Neuroimage.* 2002;16.
39. Andrade R. Serotonergic regulation of neuronal excitability in the prefrontal cortex. *Neuropharmacology.* 2011;61:382–386.
40. Ullmer C, Schmuck K, Kalkman HO, Lübbert H. Expression of serotonin receptor mRNAs in blood vessels. *FEBS Lett.* 1995;370:215–221.
41. Gamoh S, Hisa H, Yamamoto R. 5-hydroxytryptamine receptors as targets for drug therapies of vascular-related diseases. *Biol Pharm Bull.* 2013;36:1410–1415.
42. Roseman L, Leech R, Feilding A, Nutt DJ, Carhart-Harris RL. The effects of psilocybin and MDMA on between-network resting state functional connectivity in healthy volunteers. *Front Hum Neurosci.* 2014;8:204.
43. Yakovlev DS, Spasov AA, Mal'tsev DV, Anisimova VA. Effect of 5-HT(2A) receptor antagonists on blood flow in the carotid vessels upon elevation of serotonin level. *Bull Exp Biol Med.* 2014;157:350–352.
44. Buchborn T, Lyons T, Song C, Feilding A, Knöpfel T. The serotonin 2A receptor agonist 25CN-NBOH increases murine heart rate and neck-arterial blood flow in a temperature-dependent manner. *J Psychopharmacol.* 2020;34:786–794.
45. Attwell D, Laughlin SB. An energy budget for signaling in the grey matter of the brain. *J Cereb Blood Flow Metab.* 2001;21:1133–1145.
46. Seeley WW, Menon V, Schatzberg AF, et al. Dissociable intrinsic connectivity networks for salience processing and executive control. *J Neurosci.* 2007;27:2349–2356.
47. Olsen CM. Natural rewards, neuroplasticity, and non-drug addictions. *Neuropharmacology.* 2011;61:1109–1122.
48. Phan KL, Wager T, Taylor SF, Liberzon I. Functional neuroanatomy of emotion: a meta-analysis of emotion activation studies in PET and fMRI. *Neuroimage.* 2002;16:331–348.
49. Sumnall HR, Cole JC, Jerome L. The varieties of ecstatic experience: an exploration of the subjective experiences of ecstasy. *J Psychopharmacol.* 2006;20:670–682.
50. Pfaus JG, Tse TL, Werk CM, et al. Enhanced synaptic responses in the piriform cortex associated with sexual stimulation in the male rat. *Neuroscience.* 2009;164:1422–1430.
51. Weber ET, Andrade R. Htr2a gene and 5-HT(2A) receptor expression in the cerebral cortex studied using genetically modified mice. *Front Neurosci.* 2010;4:36.
52. Puig MV, Gulledge AT. Serotonin and prefrontal cortex function: neurons, networks, and circuits. *Mol Neurobiol.* 2011;44:449–464.